A femtosecond velocity map imaging study on *B*-band predissociation in CH_3I. II. The 2_0^1 and 3_0^1 vibronic levels

G. Gitzinger,[1,2] M. E. Corrales,[1] V. Loriot,[1,2] R. de Nalda,[2] and L. Bañares[1,a)]
[1]*Departamento de Química Física I, Facultad de Ciencias Químicas, Universidad Complutense de Madrid, 28040 Madrid, Spain*
[2]*Instituto de Química Física Rocasolano, CSIC, C/Serrano, 119, 28006 Madrid, Spain*

(Received 28 November 2011; accepted 20 January 2012; published online 16 February 2012)

Femtosecond time-resolved velocity map imaging experiments are reported on several vibronic levels of the second absorption band (*B*-band) of CH_3I, including vibrational excitation in the ν_2 and ν_3 modes of the bound $^3R_1(E)$ Rydberg state. Specific predissociation lifetimes have been determined for the 2_0^1 and 3_0^1 vibronic levels from measurements of time-resolved $I^*(^2P_{1/2})$ and CH_3 fragment images, parent decay, and photoelectron images obtained through both resonant and non-resonant multiphoton ionization. The results are compared with our previously reported predissociation lifetime measurements for the band origin 0_0^0 [Gitzinger *et al.*, J. Chem. Phys. **132**, 234313 (2010)]. The result, previously reported in the literature, where vibrational excitation to the C-I stretching mode (ν_3) of the CH_3I $^3R_1(E)$ Rydberg state yields a predissociation lifetime about four times slower than that corresponding to the vibrationless state, whereas predissociation is twice faster if the vibrational excitation is to the umbrella mode (ν_2), is confirmed in the present experiments. In addition to the specific vibrational state lifetimes, which were found to be 0.85 ± 0.04 ps and 4.34 ± 0.13 ps for the 2_0^1 and 3_0^1 vibronic levels, respectively, the time evolution of the fragment anisotropy and the vibrational activity of the CH_3 fragment are presented. Additional striking results found in the present work are the evidence of ground state $I(^2P_{3/2})$ fragment production when excitation is produced specifically to the 3_0^1 vibronic level, which is attributed to predissociation *via* the *A*-band $^1Q_1$ potential energy surface, and the indication of a fast adiabatic photodissociation process through the repulsive *A*-band $^3A_1(4E)$ state, after direct absorption to this state, competing with absorption to the 3_0^1 vibronic level of the $^3R_1(E)$ Rydberg state of the *B*-band. © *2012 American Institute of Physics*. [http://dx.doi.org/10.1063/1.3683252]

I. INTRODUCTION

Photodissociation of CH_3I has been extensively investigated, both experimentally and theoretically, over the years, because its apparently simple structure makes it an ideal model for the study of multichannel photodissociation processes in polyatomic molecules in which, in addition, non-adiabatic effects are important. Most of these studies have concentrated on the first absorption band (the *A*-band), characterized by a broad structureless spectrum, which results in a fast direct photodissociation and causes population inversion between the spin-orbit excited state of the iodine atom $I^*(^2P_{1/2})$ and the ground state atom $I(^2P_{3/2})$.[1–9]

The next UV absorption system in CH_3I, found in the vicinity of 200 nm, is known as the *B*-band. It consists of transitions from a non-bonding $5p\pi$ orbital of the I atom to 6*s* bound molecular Rydberg orbitals. Upon such excitation the molecule predissociates due to crossings with repulsive states, and therefore the spectrum shows clear vibrational structure[10–14] with peaks that are lifetime broadened. This system has historically received much less attention than the *A*-band, but a number of works have appeared in the literature recently[15–17] mainly exploring the details of the fast predissociation process. Also very recently, Alekseyev *et al.*[18] published new *ab initio* potential energy curves and transition moments in one dimension (1D) (minimal energy paths with respect to the umbrella angle) on this system. They found that the *B*-band is dominated by the perpendicular $^3R_1 \leftarrow XA_1$ transition and that the main predissociation channel occurs via interaction with the repulsive $4E(^3A_1)$ state, which asymptotically yields spin-orbit excited iodine atoms: $I^*(^2P_{1/2}) + CH_3$. Through their calculations, they predict that the only route to produce ground-state iodine atoms from CH_3I photodissociation in the *B*-band should be found above 55 000 cm^{-1} excitation (below 182 nm) via interaction with the $^1Q(E)$ valence state. This finding is consistent with the $I^*(^2P_{1/2})$ yield experimentally found to be unity in recent studies.[15,16,19]

One of the most interesting aspects of the *B*-band system is the fact that the details of the curve crossings between the bound Rydberg states and the repulsive states should have profound influences on the outcome of the process, so that significant differences in the dynamics should be found between different vibrational levels of the optically active $^3R_1$ state. Early Raman scattering experiments[20,21] seemed to indicate the opposite, since the same predissociation rates were extracted for all vibronic excitations, although in a later contribution[22] the authors did report a longer lifetime for excitation in the ν_3 mode and a significantly shorter

a)Electronic mail: banares@quim.ucm.es.

lifetime for excitation in the ν_1 level. However, uniform lifetimes for all vibronic levels were extracted from spectral data (linewidths) by Syage.[23] The time-resolved work of Baronavski and Owrustky[10] provided the first direct measurements of the lifetimes of many vibrational levels of the *B*-band and concluded that the lifetimes could be as extreme as 200 fs (for the $\nu_6 = 2$ level) and 4100 fs (for the $\nu_3 = 1$ level). Even though the lifetime found for the vibrationless level has been measured recently[15–17] and found in agreement with Baronavski and Owrustky's value, no other measurement of the lifetimes for the rest of the vibronic levels has been reported. We partially cover this matter in this work with measurements of the lifetimes of the $\nu_2 = 1$ and $\nu_3 = 1$ levels through a variety of time-resolved techniques.

Even stronger uncertainty remained as to the nature of the products of the predissociation process as a function of the vibronic level initially excited, since very scarce information is available on the matter, and it concerns only either the band origin[15–17] or the 2_0^2 band, since this last one can be accessed through the well known ArF laser transition at 193.3 nm.[19,24] Theoretical information is also scarce, the most valuable source at present being the very recent 1D work by Alekseyev *et al.*[18] The experimental results that will be shown in this paper tackle the two main issues of importance: the degree and nature of vibrational excitation in the methyl fragment resulting from the predissociation process, and whether the branching ratio between the spin-orbit excited and the ground-state iodine channels, defined as $\Phi^* = [I^*]/([I] + [I^*])$, is unity or less than unity. The angular nature of the process is also explored through the use of linearly polarized laser fields and a position-sensitive particle detector.

The paper is organized as follows: Section II describes the experimental setup and methodology. Section III presents the most important results and the section is organized in three parts: the first one presents time-resolved measurements of the parent molecule decay when excited in the 0_0^0, 2_0^1, and 3_0^1 transitions; the second one is a extensive study of the internal energy content of the methyl and iodine fragments appearing upon dissociation. This section is divided in two: a first part covering the simpler 2_0^1 band, and a second part describing the results for the more complex 3_0^1 band. Finally, complementary photoelectron data for the 0_0^0 and 3_0^1 transitions are shown in the third part. The results are discussed in Sec. IV and the paper closes in Sec. V with the main conclusions. An Appendix has been included at the end of the paper presenting the details of the multidimensional fitting procedure employed to analyze the complex ion images measured as a function of time delay, which has revealed to be quite important to extract all the relevant information from the images.

II. EXPERIMENTAL

The experimental setup has been described in detail in previous works[15] and only the details relevant to the present experiments will be given here. Briefly, the femtosecond laser system, a chirped pulse amplified Ti:sapphire, delivers 3.5 mJ pulses of 50 fs duration at 1 kHz repetition rate with a tunable central wavelength of about 800 nm. The main beam is split into two arms, one of which pumps an optical parametric amplifier which, followed by frequency mixing, yields pulses centered at 304.5 nm or 325–333.5 nm, with a full width at half maximum (FWHM) bandwidth of ≈ 1.7 nm, to probe I atoms or CH_3 fragments in different vibrational states, respectively, by $(2 + 1)$ resonance enhanced multiphoton ionization (REMPI).[4,5] Probe pulse energies are typically around 3–6 μJ. In some experiments, a non-resonant probe laser at the fundamental ≈ 800 nm wavelength, of about 15 μJ/pulse, was used instead of the UV probe to non-resonantly multiphoton ionize the CH_3 fragments.

The other arm is frequency quadrupled in a device consisting of a tripling unit followed by a sum-frequency mixing unit between the third harmonic and the fundamental. This arm provides the excitation (pump) radiation at about 200 nm, and allows some tuneability around this value by fine adjustments of the central wavelength of the amplifier or of the quadrupler unit. In this way, resonant radiation is produced for one-photon excitation to the 2_0^1 or 3_0^1 (or 0_0^0) vibronic transitions of the *B*-band in CH_3I, at 196.7 nm and 199.2 nm (and 201.2 nm), respectively, with a FWHM bandwidth of ≈ 0.3 nm, and typical pulse energies of <1 μJ. The linear polarization of the pump and probe laser beams is set up horizontal or vertical by means of half-wave plates and the propagation conditions are controlled through adjustable telescopes. Pump and probe beams are propagated collinearly and finally focused with a 25 cm focal length lens into a vacuum chamber where they interact with a pulsed molecular beam. The temporal delay between the pulses is controlled by a motorized delay stage placed in the probe arm, with a minimum accessible step of ≈ 1 fs. The instrument temporal response time, considered as the temporal cross correlation of the pump and probe pulses, was measured through multiphoton ionization of Xe, obtaining a value of ≈ 400 fs.

The pulsed molecular beam is composed as follows: CH_3I, kept at a temperature of 0 °C, is seeded in Ar or He, at a typical total pressure of 1.5–2.5 bars, depending on signal levels, and expanded into vacuum through a 0.5 mm nozzle diameter, 1 kHz homemade piezoelectric pulsed valve.[6] The molecular beam passes through a 1 mm diameter skimmer that separates the source chamber from the ionization chamber. We avoid clustering conditions in the beam by keeping low enough pressure and working on the initial part of the molecular beam pulse; no evidence of clusters has been observed in the mass spectrum when subjected to femtosecond pump or probe (or both) laser pulses.

After interaction with the laser pulses, the ions formed are extracted vertically by a set of electrostatic lenses working in velocity mapping configuration; typical repeller voltages were 5200 V, with optimum velocity mapping conditions found for $V_{extractor}/V_{repeller} = 0.76$. The field-free time-of-flight (TOF) region is 50 cm long. The detector is composed of a dual microchannel plate (MCP) in Chevron configuration, coupled to a phosphor screen. Mass selection was achieved through gating the gain in the front MCP plate. The images thus generated on the phosphor screen are recorded with a Peltier-cooled 12-bit charge-coupled device camera. Typical acquisition times for each image are 30 s, corresponding to 30 000 laser shots. The calibration of the apparatus was done by measuring the CH_3^+ image upon 268 nm

photodissociation of CH_3I and resonant multiphoton ionization of $CH_3(\nu = 0)$, and using the known kinetic energy (KE) release of the $CH_3(\nu = 0) + I^*(^2P_{1/2})$ and $CH_3(\nu = 0) + I(^2P_{3/2})$ channels. The energy resolution obtained is ≈ 100 meV in the 2.5 eV region for the CH_3^+ fragment zone and ≈ 40 meV in the 0.3 eV region for the I^+ fragment zone. Photoelectron images were detected with the same system by changing the polarity of the extraction field and introducing a μ-metal shield cylinder in the TOF chamber.

The methodology for the acquisition of delay scans is realized as follows. Once the proper wavelengths were chosen and the geometry on target optimized, including spatial pump-probe overlap, sets of images were acquired and personal computer stored as the temporal delay was scanned across the desired range. An experimental run consists of a repeated sequence (typically between 20 and 50) of such scans, and final stored images correspond to the accumulation of the complete sequence. This procedure proved very effective in the optimization of signal-to-noise ratio. Several experimental runs (4 to 5) were carried out in different days to get enough statistics and the results of the analysis were averaged out. Images were Abel inverted using the polar basis set expansion (pBasex) method.[25]

Some of the mass-selected images showed several contributions, corresponding to more than one formation channel. In these cases, a multidimensional homemade software (see Appendix) was employed to fit the sequences of images as a sum of contributions characterized by the product of a radial, an angular and a temporal function with adjustable parameters. This method separates the contributions that often show partial overlap in one or more dimensions.

III. RESULTS

In this work, the time-resolved photodynamics of the *B*-band in CH_3I has been studied using a range of approaches that will be presented in this section. Section III A will describe experiments of $(1 + 1')$ parent molecule ionization, where the CH_3I^+ parent ion population decay reflects the predissociation dynamics. Both 2_0^1 and 3_0^1 bands will be presented simultaneously, together with the corresponding results for the 0_0^0 band that had been shown earlier in Ref. 15. Section III B contains a study of the iodine and methyl fragment products of the predissociation process. These studies are carried out exploiting $(2 + 1)$ REMPI schemes existing in the 300–350 nm region both for I and CH_3, the latter in several vibrational states. The internal energy content, the angular distributions and the time-resolved characteristics of the process will be shown separately for the 2_0^1 and 3_0^1 bands. Finally, Section III C shows time-resolved photoelectron imaging experiments that have been performed for the 0_0^0 and 3_0^1 bands as further confirmation of the observed dynamics.

As was mentioned earlier, the absorption spectrum of CH_3I in the region of 200 nm (Refs. 10 and 14) contains a series of lifetime broadened peaks corresponding to the vibronic levels that are the subject of this work. The two peaks that clearly dominate the spectrum correspond to the 0_0^0 and 2_0^1 bands, at 201.2 nm and 196.7 nm, respectively. However, the peak assigned to the 3_0^1 band at 199.2 nm is much weaker

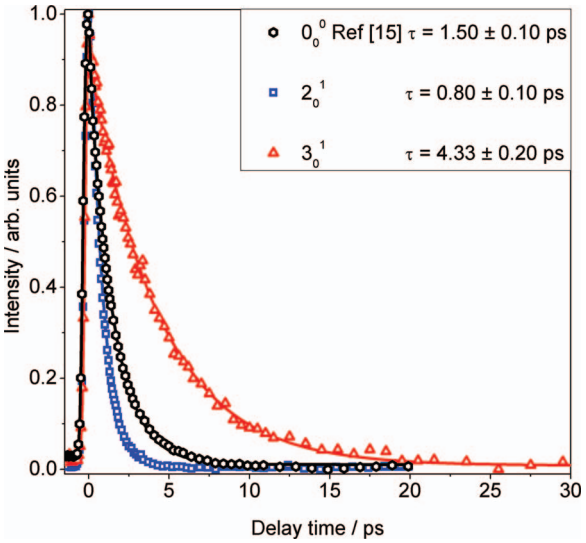

FIG. 1. Experimental transients corresponding to parent CH_3I decay after 201.2 nm (black circles, 0_0^0 band), 196.7 nm (blue squares, 2_0^1 band) and 199.2 nm (red triangles, 3_0^1 band) *B*-band excitation. Probe center wavelength was 304.5 nm. Solid lines correspond to the fit of the experimental data according to Eq. (1).

(Refs. 10 and 13). Excitation to all these levels is expected to be uncontaminated by other transitions in the present experimental conditions, where the spectral FWHM of the pump laser is around 0.3 nm.

A. Time-resolved parent decays

The CH_3I parent decay time was measured by acquiring collections of mass-selected images as a function of delay time between the pump and the probe laser pulses. Ionization of the parent CH_3I was produced through a $(1 + 1')$ REMPI scheme. Figure 1 shows transients of the CH_3I^+ signal obtained for excitation at 201.2 nm (0_0^0 band), 196.7 nm (2_0^1 band), and 199.2 nm (3_0^1 band) and photoionization with a single photon of 304.5 nm. Excitation with this $(1 + 1')$ process provides a total of 10.3 eV, i.e., 0.8 eV above the first ionization potential. Analogously to Ref. 10, the transients were fit by the sum of a Gaussian (corresponding to a time-zero enhancement of the signal, most likely related to a vertical multiphoton ionization process), and an exponential decay, convoluted with the temporal resolution function, as follows:

$$S(t) = A_1 e^{-4\ln 2[(t-t_0)/\tau_{cc}]^2} + A_2 e^{-4\ln 2(t/\tau_{cc})^2} \otimes [e^{-(t-t_0)/\tau} \times H(t - t_0)], \quad (1)$$

where τ is the lifetime of CH_3I in the *B*-band, τ_{cc} is the instrument response, t_0 is the time where pump and probe laser pulses overlap, *H(t)* is the heaviside function, and A_1 and A_2 are the amplitudes of each component. This instrument response τ_{cc} corresponds to the cross correlation between the pump and the probe pulses. This last has been measured by time-resolved photoionization of Xe and found to be ≈ 400 fs (FWHM).

The measured lifetimes, τ, obtained through these transients, are 1.50 ± 0.10 ps, 0.80 ± 0.10 ps, and 4.33 ± 0.20 ps for the 0_0^0 (Ref. 15), 2_0^1, and 3_0^1 levels, respectively. The fact

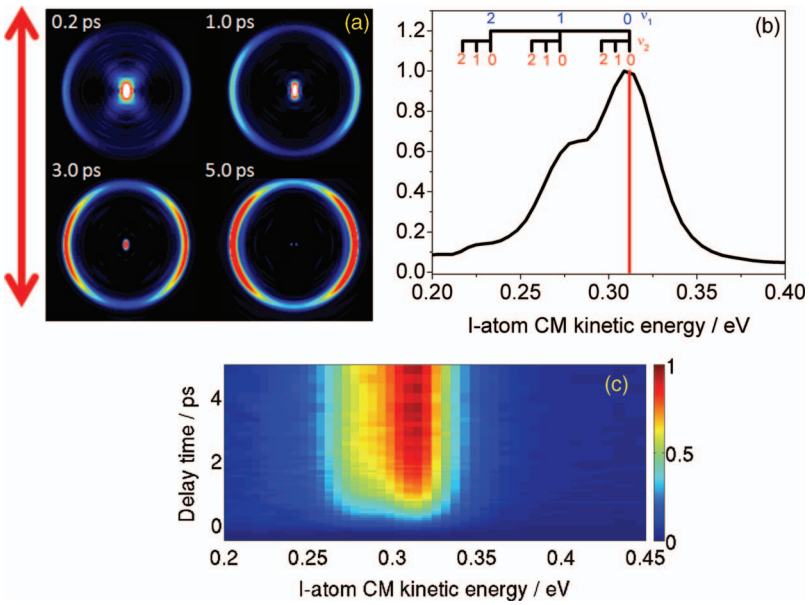

FIG. 2. (a) Sequence of Abel-inverted iodine images, in false color, for a pump-probe delay time of 0.2, 1, 3, and 5 ps for a pump laser center wavelength of 196.7 nm and a probe laser center wavelength of 304.5 nm. The double-sided arrow indicates the polarization axis of both lasers. (b) Center-of-mass kinetic energy distribution of the iodine atom from the angular integration of the image for a delay time of 5 ps. The vertical line indicates the maximum available energy and the combs give different vibrational states corresponding to the ν_1 and ν_2 modes of the CH_3 co-fragment. (c) 2D map showing the evolution of the kinetic energy distribution of the iodine fragment as a function of the delay time.

that the transient obtained for an excitation wavelength of 199.2 nm can be fitted with a single exponential, with no contamination from additional components, is an indication that excitation to the 3_0^1 band has been accomplished cleanly. The values measured in this work are consistent with those given by Baronavski and Owrustky,[10] which were 1.38 ± 0.14 ps, 1.05 ± 0.11 ps, and 4.1 ± 0.4 ps, respectively. As previously announced, lifetimes change drastically depending on the vibronic level and therefore on the pump wavelength.

B. Time-resolved fragment ion velocity map imaging

Iodine and methyl products have been measured using time-resolved mass-selected velocity map imaging for the corresponding ions resulting from the $(2+1)$ REMPI schemes that exist in the 304.5 nm region for $I(^2P_{3/2})$ and $I^*(^2P_{1/2})$, and in the 325–334 nm region for the CH_3 species in different vibrational states. The results will be presented separately for each of the *B*-band vibrational levels under study.

1. The 2_0^1 band

Time-resolved measurements of velocity map imaging (VMI) detection of the iodine atom will be shown in the first part of this section. Figure 2(a) shows a series of four Abel-inverted images corresponding to I^+ measured for different pump-probe delay times for a pump laser centered at 196.7 nm (excitation to the 2_0^1 vibronic band) and a probe laser centered at 304.5 nm ($(2+1)$ REMPI for $I(^2P_{3/2})$ and $I^*(^2P_{1/2})$ at 304.67 nm and 304.02 nm, respectively;[4] both I and I* can be ionized with the femtosecond 304.5 nm laser pulse given its bandwidth).

Two contributions are apparent in the images. The first is concentrated in the center of the image (low kinetic energy content) and can be related to dissociative ionization, probably through a process such as $CH_3I_{B-band} + nh\nu$ (304.5 nm) $\rightarrow CH_3 + I^+$, since it displays a similar temporal behavior to that of the parent ion. The second contribution is an anisotropic ring (appearing at ≈ 0.3 eV kinetic energy), whose intensity increases with time until a plateau is reached after around 5 ps. Careful analysis shows that only one single ring is observed, and it corresponds to the channel yielding the iodine atom in its spin-orbit excited state $I^*(^2P_{1/2})$. No ring associated with the channel producing ground state $I(^2P_{3/2})$ has been observed. This result is common to measurements by us and other authors in the origin 0_0^0 band,[15,17] showing a quantum yield of unity for the $I^*(^2P_{1/2})$ channel. This issue will be discussed further below.

The corresponding center-of-mass kinetic energy (KE) distribution (KER) of the iodine atom for a delay time of 5 ps between the pump and probe lasers can be seen in Fig. 2(b). The iodine peak is broad due to the contribution of several vibrational states of the CH_3 co-fragment, which give rise to a distribution of available kinetic energies. An indication of the maximum KE expected for the iodine atom for some vibrational combinations in CH_3 is represented by the combs in Fig. 2(b). A clear progression in the ν_1 symmetric stretch mode and possibly in the ν_2 umbrella mode is observed. Nevertheless, due to the poor resolution in the zone of iodine detection at 0.3 eV (≈ 40 meV), the vibrational structure could not be resolved; the vibrational activity of CH_3 will be discussed later.

Figure 2(c) depicts a 2D map representing the kinetic energy distributions for the iodine atom as a function of the delay time. The contribution at ≈ 0.3 eV corresponds to the nascent $I^*(^2P_{1/2})$ fragments. Integration of this signal is plotted as a function of time in Fig. 3(a). The curve has been fitted by a rising exponential convoluted with the temporal response

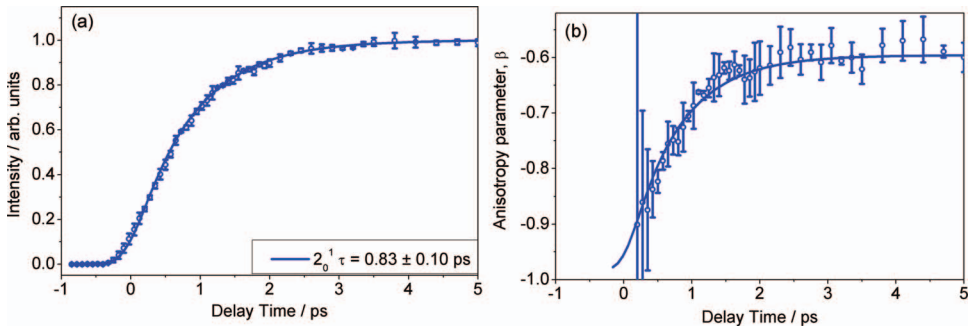

FIG. 3. (a) Experimental transient corresponding to $I^*(^2P_{1/2})$ appearance after 196.7 nm B-band excitation of CH_3I to the 2_0^1 vibronic level. (b) Experimental anisotropy transient corresponding to $I^*(^2P_{1/2})$ appearance after 196.7 nm B-band excitation of CH_3I to the 2_0^1 vibronic level. Error bars correspond to the standard deviation of each point obtained from the set of experimental runs (see Sec. II for details).

function,

$$S(t) = Ae^{-4\ln 2(\frac{t}{\tau_{cc}})^2} \otimes [(1 - e^{-\frac{t-t_0}{\tau}}) \times H(t - t_0)], \qquad (2)$$

where τ is the lifetime of CH_3I in the B-band, τ_{cc} is the instrumental response time, t_0 is the time of pump-probe temporal overlap, and A is an amplitude factor. Through this method, the lifetime of CH_3I in the 2_0^1 band is found to be 0.83 $\pm$ 0.10 ps, in agreement with the lifetime measured by detecting the parent decay (0.80 $\pm$ 0.10 ps).

Further insight can be gained by examining the angular character of this component in the I^+ image. As is expected in a situation where the effective rotational period of the molecule is comparable with the lifetime of the excited state, the angular distribution of the I^+ signal changes with pump-probe delay time. All images in Fig. 2 show perpendicular character, but the degree of anisotropy evolves in time. In Fig. 3(b), the points represent the anisotropy parameter β extracted from a fit of each angular dependence according to the equation $I(\theta) = \sigma/4\pi[1 + \beta P_2(\cos\theta)]$ (Ref. 26), where σ is the total absorption cross section, θ is the angle between the polarization axis and the fragment velocity vector, and $P_2(\cos\theta)$ is the second Legendre polynomial. In principle, aligned I-atoms can be produced in the predissociation process and thus higher order terms (including β_4 and β_6) have to be considered in the above equation as additional terms. However, for linearly polarized light and (2 + 1) REMPI detection, the $I^*(^2P_{1/2})$ atoms cannot be aligned or oriented because the populations of the $M_J = \pm 1/2$ levels must be equal.[27] As can be observed, for early times $\beta \approx -1$, as is expected for a perpendicular transition, but this extreme anisotropy is lost with time, and β evolves towards an asymptotic value of approximately -0.6 ± 0.1. If this behavior is fitted with an exponential function, analogous to Eq. (2), a characteristic time of 0.75$\pm$0.1 ps is obtained. These results are similar to those observed for the anisotropy measured from the I^+ images when CH_3I is excited to the 0_0^0 band (see Fig. 2(b) in Ref. 15). An estimate of the loss of anisotropy due to molecular rotation can be derived from a semiclassical model.[28,29] According to this model, an asymptotic value of the anisotropy parameter of -0.6 is compatible with a rotational temperature of the molecular sample of about 30 K, which seems quite reasonable considering the supersonic expansion producing the CH_3I molecular beam in our experiment.

Direct detection of the CH_3 co-fragment provides additional information. Time-resolved VMI measurements of CH_3 have been carried out and are shown below. The (2 + 1) REMPI schemes exploiting the two-photon resonance for the $3p_z(^2A_2'' \leftarrow {}^2A_2'')$ transition in CH_3 are employed.[5] For these, the probe laser has been centered at the wavelengths of 333.5 nm, 329.4 nm, or 325.8 nm for the study of the CH_3 0_0^0, 2_1^1, and 2_2^2 bands of the transition. This allows for independent exploration of vibrational activity in the ν_2 (umbrella) mode of nascent CH_3. As will be shown, activity in the ν_1 (symmetric stretch) mode can also be studied due to the spectral proximity to the unexcited band and to the broad spectrum of the probe laser pulse.

Figure 4(a) shows four mass-selected images for CH_3 at selected pump-probe delay times for a probe laser center

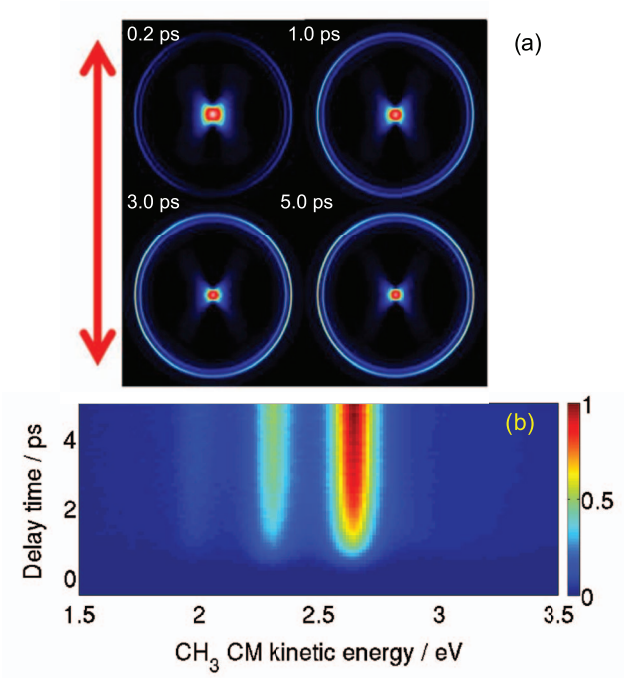

FIG. 4. (a) Sequence of Abel-inverted methyl images, in false color, for a pump-probe delay time of 0.2, 1, 3, and 5 ps for a pump laser center wavelength of 196.7 nm for B-band excitation of CH_3I to the 2_0^1 vibronic level and a probe laser center wavelength of 333.5 nm. The double-sided arrow indicates the polarization axes of both lasers. (b) 2D map of the KE distribution of the CH_3 fragment as a function of the delay time.

wavelength of 333.5 nm. The images show three rings (in decreasing order of intensity from the outer to the inner ring) that can be assigned to $CH_3(\nu = 0)$ (outer ring), $CH_3(\nu_1 = 1)$ (middle ring), and $CH_3(\nu_1 = 2)$ (inner ring), always in correlation with $I^*(^2P_{1/2})$. It is important to note that no indication of a component in correlation with ground-state iodine $I(^2P_{3/2})$ has been found, in agreement with the direct iodine measurements shown above. As was mentioned before, CH_3 excited in the ν_1 mode can be detected because of the spectral proximity of the 1_1^1 and 1_2^2 bands to the target 0_0^0 band. Angular integration provides the kinetic energy distributions, and the complete measurement is shown in Fig. 4(b) in the form of a 2D map containing the CH_3 KE distributions as a function of time.

As was done for the I^+ images shown above, further insight can be gained by examining the angular character of the different components in the CH_3^+ images. In contrast with the I-atom angular distributions, that were fitted using just one overall anisotropy parameter β, in the case of CH_3, it was necessary to use β_2 and β_4 anisotropy parameters for good fitting ($\beta_6 \approx 0$ in all cases), according to the equation $I(\theta) = \sigma/4\pi[1 + \beta_2 P_2(\cos\theta) + \beta_4 P_4(\cos\theta) + \beta_6 P_6(\cos\theta)]$, where P_2, P_4, and P_6 are the second, fourth, and sixth order Legendre polynomials. Similarly to the I-atom angular distributions, the CH_3 angular distributions change with pump-probe delay time. However, at variance with the I-atom angular distribution which shows a β_2 parameter close to the -1 limiting value for a perpendicular transition at the shortest delay times and then β evolves to approximately -0.6 ± 0.1 at long enough delay times (here $\beta_4 = 0$; see above), in the case of the CH_3 main component ($\nu = 0$) angular distribution, β_2 varies from -0.52 at the shortest delay time up to -0.04 at asymptotic delay times and β_4 changes from -0.11 up to -0.07. The time-dependent behavior of β_2 and β_4 is shown in Fig. 5. This same complex behavior has been observed by Blanchet and co-workers[17] and has been assigned to CH_3 fragment rotational alignment. Work is in progress in our group to perform a quantitative analysis of the anisotropy of the CH_3 fragment, which includes measurements at different polarization geometries of the pump and probe lasers.

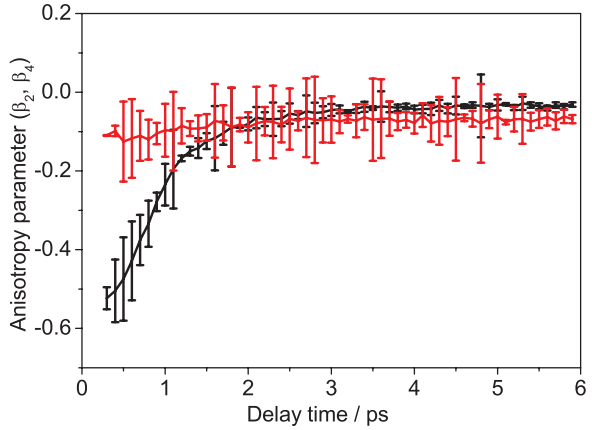

FIG. 5. Time dependence of the β_2 (black) and β_4 (red) anisotropy parameters for the $CH_3(\nu = 0)$ fragments arising from the predissociation of CH_3I from the 2_0^1 vibronic level.

As mentioned above, vibrational activity in CH_3 has been explored by tuning the probe laser center wavelength to the center of the 0_0^0, 2_1^1, and 2_2^2 bands of the 2-photon $3p_z(^2A_2'' \leftarrow {}^2A_2'')$ transition employed for REMPI. The three KE distributions resulting from those experiments, carried out for a long delay time (10 ps) between the pump and the probe laser pulses, are shown in Fig. 6(a).

In order to obtain quantitative estimates of the degree of vibrational activity in nascent CH_3, ion images of this fragment were also acquired by probing with a short, non-resonant laser pulse centered at ≈ 800 nm to produce ionization in a multiphoton ionization (MPI) process. The corresponding images showed a similar overall structure, except with the contributions broadened in energy, as is expected due to the lack of selectivity of the vibrational state of the product fragment. The method has consisted of finding the best fit to the non-resonant KE distribution curve by optimization of the weights of the individual resonant contributions. The curve obtained from this procedure is shown, in comparison with the experimental non-resonant result, in Fig. 6(b).

Table I shows the CH_3 vibrational states that have been detected, together with the estimates of relative populations obtained through this method. The method assumes that the excitation efficiency is the same for all transitions observed, which need not be the case. However, the fact that a good fit has been found to the non-resonant probe result, indicates that the assumption is reasonable. In any case, the relative populations thus extracted, shown in Table I, must be understood qualitatively. As can be seen, vibrational activity into the ν_1 mode of CH_3 increases quite substantially when *B*-band excitation is produced to the 2_0^1 vibronic level in comparison with excitation to the band origin (0_0^0). In the case of CH_3 detection centered at the 2_1^1 and 2_2^2 bands, the additional inner rings in the images (lower energy peaks in the KE distributions) are assigned to ν_1, ν_2 combination bands, whose populations are also included in Table I.

Integration of each of the components of the CH_3 signal for a range of pump-probe delays yields a collection of transients, i.e., signal magnitude as a function of time, that are shown in Fig. 7. The curves have been fitted by an exponential function convoluted with the temporal

TABLE I. Vibrational levels observed in the ground electronic state of CH_3 in correlation with $I^*(^2P_{1/2})$ appearing upon *B*-band predissociation of CH_3I from different vibronic levels, with estimated relative populations (±10%). See text for more details.

$CH_3(\nu_1,\nu_2)$		*B*-band	vibronic level	
ν_2	ν_1	0_0^0 (Ref. 15)	2_0^1	3_0^1
0	0	37	34	29
0	1	7	23	20
0	2	<1	4	7
1	0	28	25	15
1	1	4	9	8
1	2	<1	<1	2
2	0	24	5	12
2	1	<1	<1	6
2	2	<1	<1	1

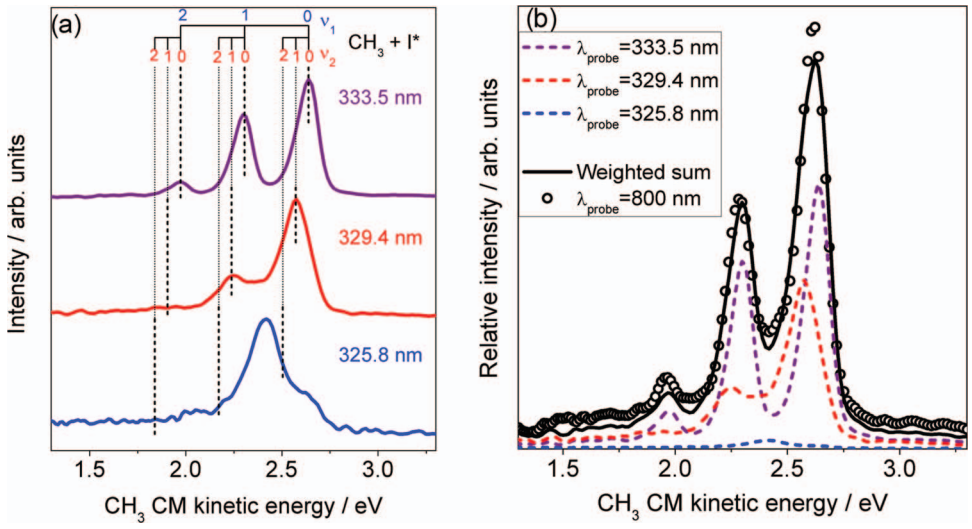

FIG. 6. (a) CM CH_3 KE distributions measured at a pump-probe delay time of 10 ps, with a pump laser centered at 196.7 nm for *B*-band excitation of CH_3I to the 2_0^1 vibronic level and a probe laser centered at 333.5 nm (top), 329.4 nm (middle), and 325.8 nm (bottom), in resonance with the *Q* branch of the two-photon $3p_z(^2A_2'' \leftarrow {}^2A_2'')$ transition in CH_3 in its 0_0^0, 2_1^1, or 2_2^2 bands, respectively. (b) CM CH_3 KE distribution upon *B*-band excitation of CH_3I at 196.7 nm to the 2_0^1 vibronic level and subsequent CH_3 non-resonant MPI probing with pulses centered at $\approx$800 nm delayed by 10 ps (open circles). Colored lines contain the resonant probing distributions shown in the left panel, at 333.5 nm (dashed purple), 329.4 nm (dashed red), and 325.8 nm (dashed blue). The solid black line is the distribution obtained through the weighted sum of the three KE distributions for resonant CH_3 probing.

response function (see Eq. (2)). The characteristic risetimes, obtained separately for each state, are summarized in Table II along with the lifetimes obtained from the parent decay and the I-atom transients. As can be expected, no differences in the lifetimes of the $CH_3(\nu)$ products could be observed. The values are also totally consistent with those obtained from the measurement of the parent decay and iodine appearance presented in Secs. III A and III B 1.

2. The 3_0^1 band

The 3_0^1 band represents a more challenging case. As is clear from the absorption spectra reported in Refs. 10 and 14 this vibronic band, centered at 199.2 nm, shows very low absorption compared to the 0_0^0 and 2_0^1 bands. Signals are considerably lower in this case, and more ample statistics are necessary. Also, care must be taken in order to ensure that the least possible contamination from nearby bands is occurring. Time-resolved experiments have been performed for the excitation in this level similarly to what has been described for the 2_0^1 band, and the results will be presented in the same order.

TABLE II. Lifetimes (in ps) observed upon *B*-band excitation of CH_3I in the 0_0^0, 2_0^1, and 3_0^1 levels obtained from the different experiments carried out in the present work.

	Vibronic level		
Detection method	0_0^0	2_0^1	3_0^1
$I^*(^2P_{1/2})$ fragment	1.52 ± 0.10	0.83 ± 0.10	4.45 ± 0.30
Parent ion	1.50 ± 0.10	0.80 ± 0.10	4.33 ± 0.20
$CH_3(\nu = 0)$	1.44 ± 0.14	0.85 ± 0.16	...
$CH_3(\nu_1 = 1)$	1.57 ± 0.18	0.78 ± 0.10	...
$CH_3(\nu_1 = 2)$	...	0.92 ± 0.24	...
$CH_3(\nu_2 = 1)$	1.57 ± 0.20	0.88 ± 0.10	...
$CH_3(\nu_1 = 1; \nu_2 = 1)$	1.76 ± 0.25	0.92 ± 0.10	...
$CH_3(\nu_1 = 2; \nu_2 = 1)$	...	0.88 ± 0.18	...
$CH_3(\nu_2 = 2)$	1.42 ± 0.20	0.85 ± 0.14	...
$CH_3(\nu_1 = 1; \nu_2 = 2)$	1.53 ± 0.20	0.90 ± 0.21	...
Photoelectrons	1.57 ± 0.20	...	4.30 ± 0.20
Average values	1.52 ± 0.05	0.86 ± 0.04	4.34 ± 0.13

Figure 8(a) shows the evolution of the kinetic energy distribution measured for the I-atom appearance as a function of delay time for excitation at 199.2 nm (3_0^1 band) extracted from the corresponding I^+ images. In these experiment, the probe laser is centered at 304.5 nm ((2 + 1) REMPI for $I(^2P_{3/2})$ and $I^*(^2P_{1/2})$; see above). Similarly to the observations for the 2_0^1 band, the main component of the iodine images for long pump-probe delay times is an anisotropic ring at $\approx$0.3 eV, of perpendicular character, that can be mainly assigned to the formation of iodine in its spin-orbit excited state $I^*(^2P_{1/2})$. This component is relatively broad in energy and can be seen in the range of 0.25–0.35 eV. The intensity of this ring increases with time until a plateau is reached after around 15 ps. It is signaled on the 2D maps of Fig. 8(a) with a red arrow. Another component is present in the central part of the image (i.e., low kinetic energy), but, in contrast to the observations for the 2_0^1 band, in this case this component is extremely short-lived (only present during pump-probe temporal overlap). It is indicated on the map with a blue arrow. We believe this component is related to multiphoton dissociative ionization processes yielding $CH_3 + I^+$. No low-KER component with a measurable decay time, such as observed for 2_0^1, is detected in this case, possibly due to the low absorption for the 3_0^1 band.

The iodine images for this vibronic band possess, however, greater complexity when compared to the 2_0^1 band, showing an additional component consisting of an energetically narrow contribution appearing at $\approx$0.3 eV, indicated on the map with a yellow arrow. This component grows very fast and

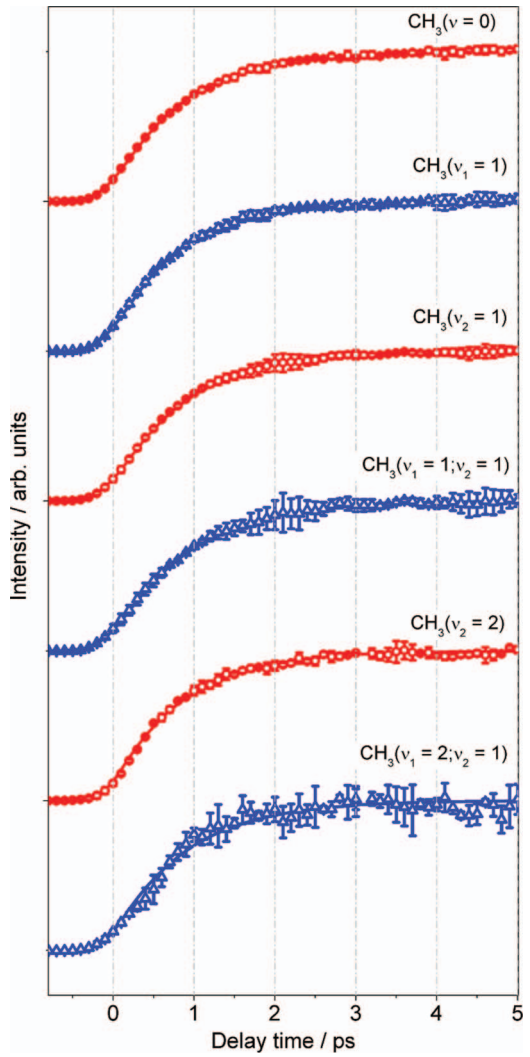

FIG. 7. Experimental transients corresponding to the $CH_3(\nu_1, \nu_2)$ fragment appearance after 196.7 nm *B*-band excitation of CH_3I to the 2_0^1 vibronic level. Each curve corresponds to the integration of a population component of the CH_3 signal (see text). The lines are fits to the data according to Eq. (2). All risetimes obtained are compatible within errors. Error bars correspond to the standard deviation of each point obtained from the set of experimental runs (see Sec. II for details).

reaches a plateau at ≈ 0.5 ps. Only a global 3D analysis of the measurements (see Appendix) has permitted the observation of this component, since it is about two orders of magnitude weaker than the main, broad component at 0.3 eV.

For a long delay time between the pump and probe pulses (asymptotic situation), the kinetic energy distribution of iodine essentially contains the broad contribution around 0.3 eV, that can be seen in Fig. 8(b). For this figure, angular integration has only been performed in the range of $\pm 20^\circ$ around the equator to avoid as much as possible the contribution from strong signal in the center of the image. From these results, it is clear that in this band vibrational activity in the CH_3 co-fragment is higher than for the 2_0^1 band (it is interesting to compare with Fig. 2(b)). It is also noteworthy that the distribution presents a possible component with kinetic energy in excess of the available energy for the $I^*(^2P_{1/2})$ channel, beyond instrument resolution (compare again with Fig. 2(b)). From this observation, together with the methyl results that will be presented below, this component has been assigned to the detection of a ground state $I(^2P_{3/2})$ channel, visible upon excitation at this wavelength. This point will be discussed further below.

Integration of each of the components at ≈ 0.3 eV yields temporal transients that are shown in Fig. 9(a). The discrimination of the two components has only been possible through the use of the 3D fitting procedure described in Appendix. Lifetimes are found to be 0.17 ± 0.1 ps and 4.45 ± 0.3 ps for the fast and slow signals, respectively. It is clear that the main, slow component corresponds to iodine resulting from CH_3I predissociation from the 3_0^1 band, with a lifetime that is compatible with that obtained from parent decay measurements in Sec. III B 1 (4.33 ± 0.20 ps). In addition, the β parameter of the fast component remains unchanged and is equal to -1 while the initial and final values of β for the slow component are found to be -1 and -0.62. Once again, the latter temporal change of the anisotropy parameter β has been fitted with a function of the form Eq. (2) and a characteristic time of 3.73 ± 0.3 ps has been found (Fig. 9(b)), slightly lower than the lifetime of the excited state.

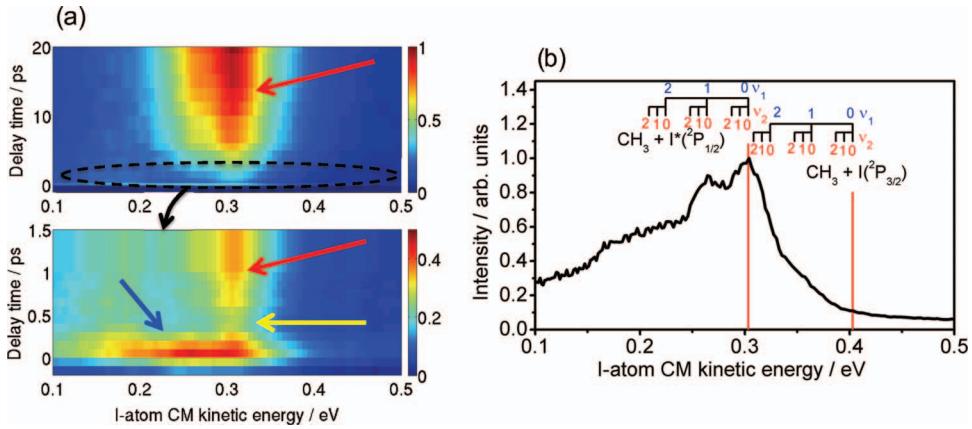

FIG. 8. (a) 2D map showing the evolution of the KER of the iodine fragment as a function of the delay time from 0 up to 20 ps (top) and up to 1.5 ps (bottom) for the 3_0^1 band. The three components that are described in the text are indicated with colored arrows. Red arrow: Main, broad component, with slow temporal rise, centered around 0.3 eV. Yellow arrow: Energetically narrow component around 0.3 eV with a rapid temporal rise. Blue arrow: Energetically broad component observed only during the temporal overlap of the two lasers. (b) Kinetic energy distribution of the iodine atom for a long delay time (30 ps) between the pump and probe pulses. Integration has been performed only for the angular range of $\pm 20^\circ$ around the equator (see text for details). Maximum kinetic energies expected for several channels are indicated.

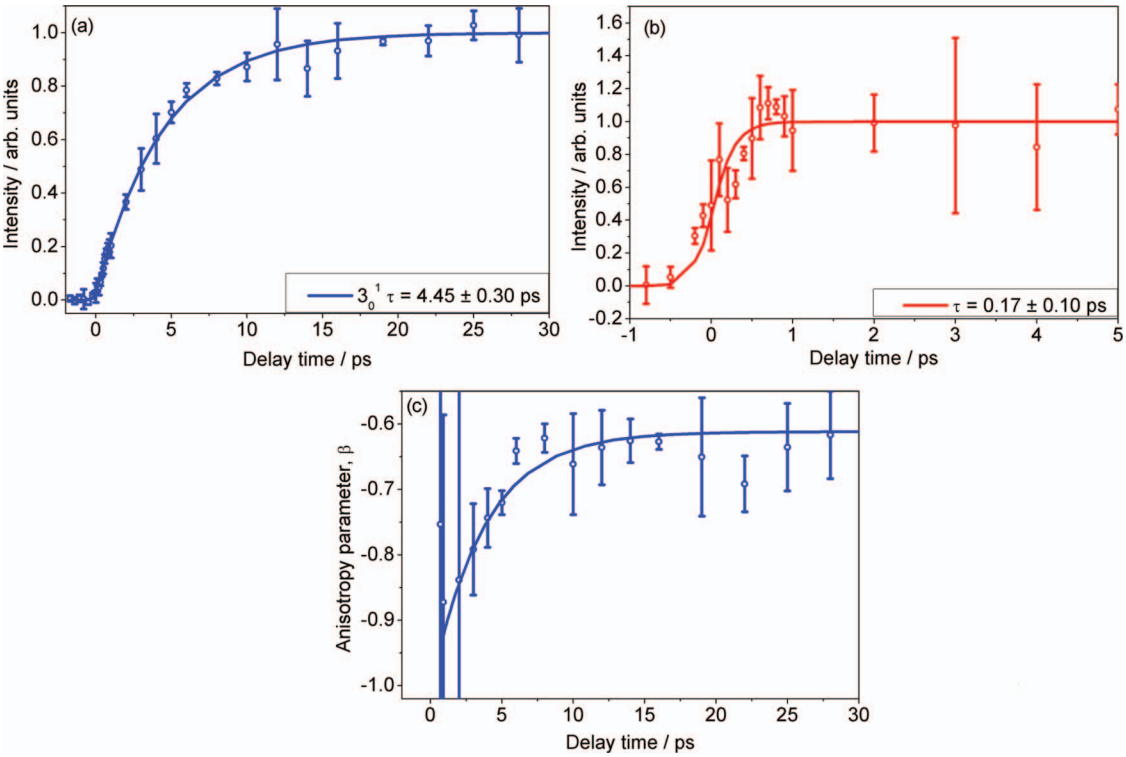

FIG. 9. (a) Experimental transient corresponding to the iodine atom appearance after 199.2 nm excitation of CH_3I (slow component). (b) Same as (a), but for the fast component. (c) Anisotropy parameter β of the iodine signal (slow component) as a function of time. Fits have been performed using the functional form of Eq. (2), with characteristic times of 4.45 ± 0.3 ps, 0.17 ± 0.1 ps, and 3.73 ± 0.3 ps for the slow component, the fast component, and the change of the anisotropy parameter, respectively. Error bars correspond to the standard deviation of each point obtained from the set of experimental runs (see Sec. II for details).

Dynamics upon 3_0^1 *B*-band excitation in CH_3I can be explored further by direct measurement of the CH_3 fragment, as was done for the 2_0^1 case. Similarly, VMI measurements of CH_3 have been performed using the $(2+1)$ REMPI schemes through the $3p_z(^2A_2'' \leftarrow {}^2A_2'')$ transition with probe laser wavelengths of 333.5 nm, 329.4 nm, or 325.8 nm for the use of the 0_0^0, 2_1^1, and 2_2^2 bands of the transition.

A contrast-enhanced asymptotic image obtained for CH_3 with a probe wavelength of 333.5 nm is shown in Fig. 10(a). The image is rather similar to that detected for the 2_0^1 band (see Fig. 4(a)), with three rings that can be assigned to $CH_3(\nu = 0)$ (outer ring), $CH_3(\nu_1 = 1)$ (middle ring), and $CH_3(\nu_1 = 2)$ (inner ring), always in correlation with $I^*(^2P_{1/2})$. A higher degree of vibrational excitation is evident though in the higher intensity of the inner rings. However, an important difference must be pointed out for this case: the presence of another (much fainter) series of rings with a larger diameter (higher KER) than that corresponding to $CH_3(\nu = 0)$ in correlation with $I^*(^2P_{1/2})$. For 329.4 nm and especially for 325.8 nm probing (images not shown), this second series of rings becomes relatively more important. This can be seen more clearly in Fig. 10(b), where the asymptotic KERs are plotted. We believe that the second series of rings can be assigned to CH_3 in correlation with ground-state iodine. In this channel, CH_3 mainly appears with one quantum of excitation in the symmetric stretch mode, $\nu_1 = 1$. The implications of this finding will be explored in Sec. IV.

Similarly to the procedure described for the 2_0^1 band, non-resonant probing of nascent CH_3 was carried out with a short laser pulse at ≈ 800 nm that ionizes CH_3 in all vibrational states. The CH_3 KER thus obtained is shown in Fig. 10(c). The comparison of the results with those obtained resonantly provides estimates of the relative populations in the vibrational states of the nascent fragment, according to the method described in Sec. III B 1. The curve obtained by the weighted sum of the three KERs obtained resonantly is also shown in Fig. 10(c), together with the distribution obtained non-resonantly. The values of the estimated vibrational distributions for CH_3 are shown in Table I. This non-resonant probe experiment also allows us to provide an estimate for the I* quantum yield in the process, for which a value of 0.93 $\pm$ 0.05 has been obtained.

C. Time-resolved photoelectron velocity map imaging

Time-resolved photoelectron velocity map imaging experiments have been performed for the 0_0^0 and 3_0^1 vibronic levels of the *B*-band. These experiments were designed to provide a more complete picture of the process, especially in the case of the more complex 3_0^1 band. In all cases, a short pump pulse centered at the wavelength of the vibronic transition under study, and a short probe pulse centered at 304.5 nm (resonant ionization of iodine and non-resonant ionization of CH_3I and CH_3) were employed.

Figure 11 shows the recorded images for different pump-probe delay times for a pump laser centered at a wavelength of 201.2 nm (left, 0_0^0 band) and 199.2 nm (right, 3_0^1 band) and a probe laser centered at 304.5 nm. At pump-probe

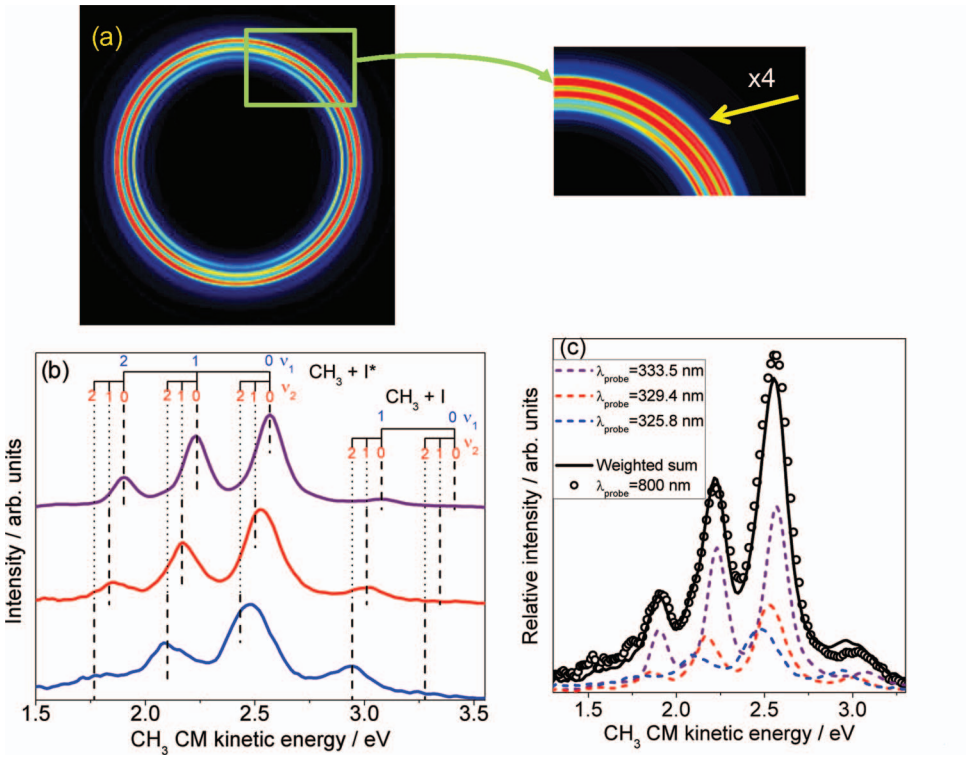

FIG. 10. (a) Abel-inverted CH_3^+ image, in false color, obtained upon 199.2 nm excitation of CH_3I (3_0^1 band) and 30 ps delayed 333.5 nm probing of CH_3 (0_0^0 band of the fragment). The contrast of the image has been increased in order to appreciate the details better. The inset to the right corresponds to a 4× contrast enhanced portion of the image shown to the left to better appreciate the outer weak ring (indicated with the yellow arrow). (b) CM CH_3 KE distributions recorded at a pump-probe delay of 30 ps, with a pump laser centered at 199.2 nm (3_0^1 band) and a probe laser centered at 333.5 nm (top), 329.4 nm (middle), and 325.8 nm (bottom), in resonance with the Q branch of the two-photon $3p_z(^2A_2'' \leftarrow {}^2A_2'')$ transition in CH_3 in its 0_0^0, 2_1^1, or 2_2^2 bands, respectively. (c) CM CH_3 KE distribution upon B-band excitation of CH_3I at 199.2 nm and subsequent CH_3 non-resonant MPI probing with pulses spectrally centered at ≈ 800 nm delayed by 30 ps (open circles). Colored lines contain the resonant probing distributions shown in the left panel, at 333.5 nm (dashed purple), 329.4 nm (dashed red), and 325.8 nm (dashed blue). The solid black line is the distribution obtained through the weighted sum of the three KE distributions for resonant CH_3 probing.

temporal overlap, we observe a series of rings that correspond to the photoelectrons originated through ionization of CH_3I, leading to the formation of CH_3I^+ and the release of an electron. These rings gradually disappear, and for long delay times (20 ps) two new rings emerge that can be attributed to the appearance of iodine atoms. These photoelectrons are strongly enhanced due to the use of a REMPI scheme for the I-atom ionization.

From the photoelectron images above it is possible to obtain the photoelectron spectra relative to the binding energy. This is shown in Fig. 12, where the top row is acquired near temporal overlap (400 fs delay between the pump and probe pulses) for an excitation at 201.2 nm (0_0^0 band, Fig. 12(a)) or at 199.2 nm (3_0^1 band, Fig. 12(b)). At short delay times the photoelectrons are originated in the parent molecule, and therefore the photoelectron data are represented as a function of the binding energy of the electron in CH_3I. For the 0_0^0 band, the most important contribution is related to the origin band of the $CH_3I^+(E_{3/2})$ ground state. Other weaker peaks are observed, the most prominent ones corresponding to the

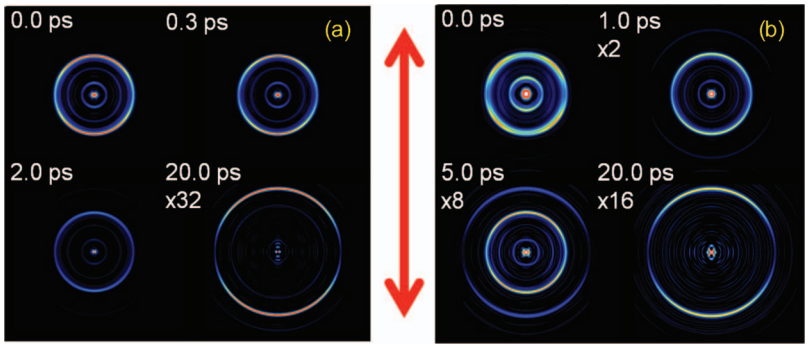

FIG. 11. Left: Sequence of Abel-inverted photoelectron images, in false color, for a pump-probe delay time of 0, 0.3, 2, and 20 ps for a pump laser center wavelength of 201.2 nm (0_0^0 band) and a probe laser center wavelength of 304.5 nm. The double-sided arrow indicates the polarization axis of both lasers. Right: Sequence of Abel-inverted photoelectron images, in false color, for a pump-probe delay time of 0, 1, 5, and 20 ps for a pump laser center wavelength of 199.2 nm (3_0^1 band) and a probe laser center wavelength of 304.5 nm. The double-sided arrow indicates the polarization axis of both lasers.

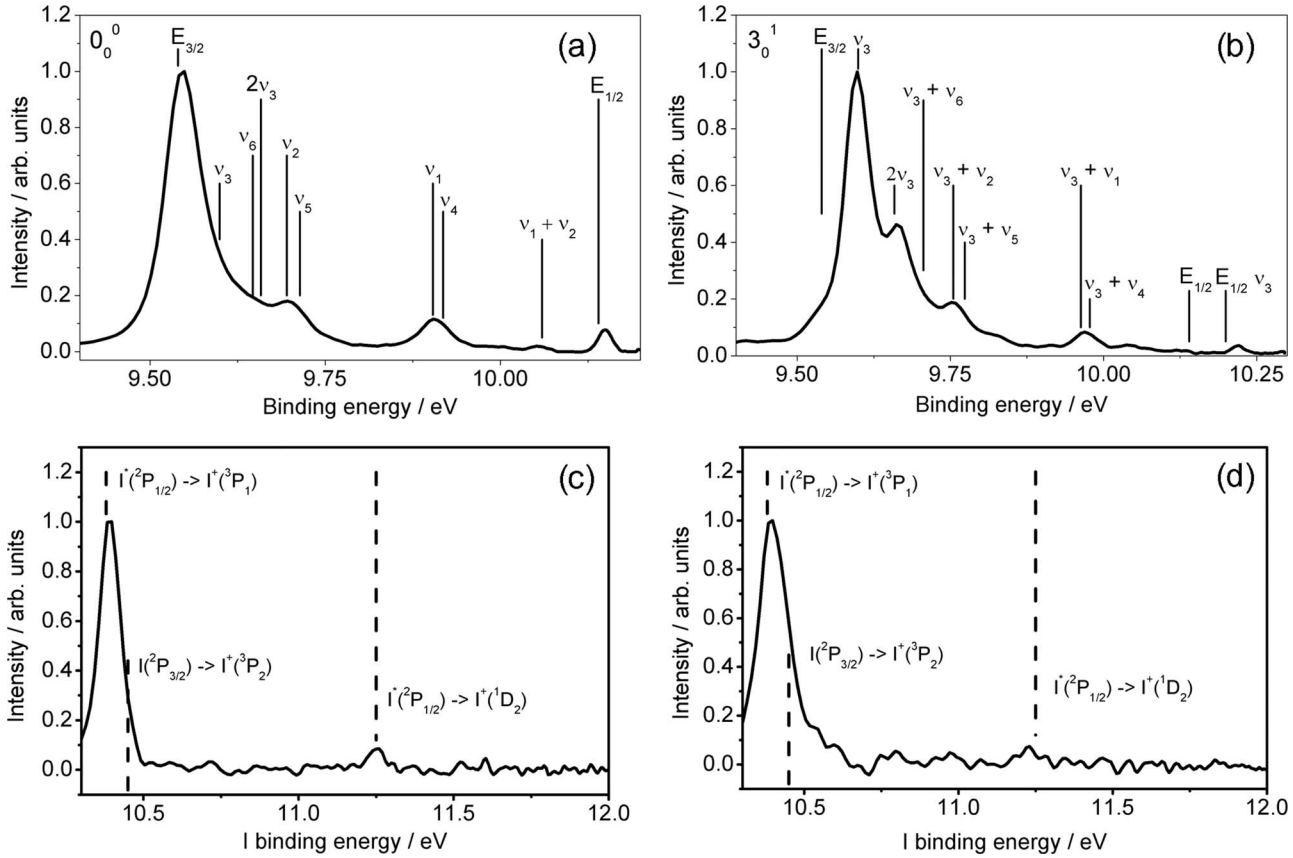

FIG. 12. Photoelectron spectra plotted relative to the binding energy. Top row: Pump-probe delay time of 400 fs (photoelectron kinetic energy distribution plotted as a function of the binding energy for the parent molecule). (a) Pump laser center wavelength of 201.2 nm (0_0^0 band). (b) Pump laser center wavelength of 199.2 nm (3_0^1 band). Bottom row: Pump-probe delay time of 30 ps (photoelectron kinetic energy distribution plotted as a function of the binding energy in the iodine product). (c) Pump laser center wavelength of 201.2 nm (0_0^0 band). (d) Pump laser center wavelength of 199.2 nm (3_0^1 band). In all cases, the probe laser center wavelength is 304.5 nm.

$CH_3I^+(E_{3/2})$ $\nu_2 = 1$, $\nu_1 = 1$, and $\nu_4 = 1$ modes. Additionally, a weak peak is seen at 10.14 eV, which could be assigned to the electronically excited ion configuration $CH_3I^+(E_{1/2})$. Even though core conservation is primarily expected,[13] we believe that this is the most likely assignment, since no vibrations correspond to this value of the binding energy. It is interesting to note that, for pump-only excitation at 201.2 nm, only the peak corresponding to the $CH_3I^+(E_{3/2})$ ground state is observed ((1 + 1) process), as had been reported in Ref. 16. These parent ion excitations had been observed in old VUV photoelectron spectra such as those reported in Ref. 30 or zero kinetic energy electron (ZEKE) measurements.[31] To our knowledge, the only previous study of photoelectrons arising from $(1 + 1')$ ionization of CH_3I using the resonant Rydberg states is the measurement of Thiré *et al.*,[16] and was performed for the origin band of the 6*s*[2] state (pump laser tuned to 201.2 nm). In that study, three different probe wavelengths (346.0 nm, 322.8 nm, and 313.0 nm) were explored and gave similar results. Our results for the 0_0^0 band, performed with a probe wavelength of 304.5 nm, yield compatible data, the only uncertainty being the assignment of the $CH_3I^+(E_{1/2})$ peak, which lies beyond their reported data.

More interesting is the case of the 3_0^1 band, with excitation at 199.2 nm, for which the photoelectron spectra changes significantly, as can be seen in Fig. 12(b). In this case, the main contribution is related to the formation of CH_3I^+ with one quantum of excitation in the ν_3 mode. Since the potential energy surface of the *B* 6*s*[2] Rydberg state is similar to the ground state surface of the ion, transitions with $\Delta\nu = 0$ are expected to dominate.[14,16] Significant population in the $\nu_3 = 1$ state of the ion is indeed expected due to initial excitation to the $\nu_3 = 1$ level of the Rydberg state. The fact that this $\nu_3 = 1$ component of the photoelectron spectrum is the main one, with practically no contribution originated in the $CH_3I^+(E_{3/2})$ $\nu = 0$, $\nu_2 = 1$, or $\nu_6 = 1$ levels is proof of the sole excitation of the $\nu_3 = 1$ vibrational state of the *B*-band upon 199.2 nm irradiation. Other vibrational combinations are visible in the spectrum, but always with at least one quantum of excitation in the ν_3 mode.

When acquired with a long delay time between the pump and probe laser pulses, the photoelectrons are originated from the iodine atoms resulting from dissociation. (2 + 1) REMPI schemes are resonant for both I and I* when a short pulse at 304.5 nm is employed. Figures 12(c) and 12(d) contain the photoelectron energy distributions, with the *x*-axis indicating the binding energy for the I atom. Evidence for I* formation is clear for both the 0_0^0 and the 3_0^1 bands; evidence for ground state I formation, on the other hand, is unclear, given that the only signature, $I(^3P_{3/2}) \rightarrow I^+(^3P_2)$, would appear to the right of the $I^*(^2P_{1/2}) \rightarrow I^+(^3P_1)$ contribution, but within the

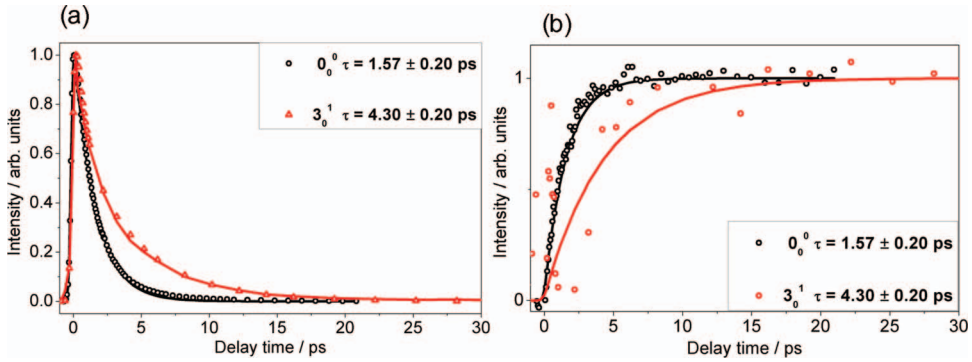

FIG. 13. (a) Experimental transients corresponding to the photoelectron signal originated from the ionization of the parent molecule after *B*-band excitation of CH_3I and ionization at 304.5 nm. (b) Same as in (a) but for the ionization of the iodine atom.

resolution of the apparatus; only a slight indication of its presence appears in the 3_0^1 data, in the form of a shoulder to the right of the main I* signal. No ground state iodine formation for the 0_0^0 band, and a minor I channel for the 3_0^1 band is expected from the ion data that were presented in the preceding section.

Since the electrons originated in CH_3I and those originating in iodine are spatially separated in the velocity map images, it is possible to perform a partial integration of the signal. This has been done for sequences of pump-probe delays and is shown in Fig. 13. Through this method, lifetimes have been found to be 1.57 ± 0.2 ps and 4.30 ± 0.2 ps for the excitation at the 0_0^0 and 3_0^1 levels, respectively, in agreement with the values obtained with ion detection techniques. This serves as a further measurement of the lifetimes and as proof of the assigned peaks in the photoelectron spectra.

As can be seen in the images depicted in Fig. 11, the angular distributions of the photoelectrons arising from the parent ion CH_3I^+ and the fragment ion I^+ are complex, especially for the former. We have fitted the angular distributions of the main ring assigned to the CH_3I^+ and of the main ring assigned to the I^+ using anisotropy parameters up to the eighth order. In general, we have found that the β_6 and β_8 parameters are close to zero at all time delays, whereas the β_2 and β_4 parameters evolve significantly with time. In the case of the CH_3I^+ photoelectrons for the 0_0^0 band, β_2 and β_4 parameters change from about 0.45 and -0.40 at zero time delay to 0.20 and 0 at about 10 ps, respectively. For the I^+ photoelectrons, β_2 and β_4 change from 0.10 to -0.10 at zero time delay to about 0.85 and -0.25 at 20 ps time delay, respectively. Qualitatively same behavior is observed for the photoelectrons when excitation is to the 3_0^1 vibronic band. Figures showing the time-evolution of the β_2 and β_4 for both the CH_3I^+ and I^+ photoelectrons upon excitation to the 0_0^0 and 3_0^1 bands are included as supplementary material.[39] It is out of the scope of the present paper a quantitative analysis and discussion of these photoelectron angular distributions.

IV. DISCUSSION

The characteristics of *B*-band predissociation in CH_3I, including lifetimes, anisotropy, branching ratio, and vibrational activity of the methyl fragments, have proven to be strongly dependent on the vibrational level of initial excitation in the parent molecule. Figure 14 shows the detail of the potential energy curves that intervene in the excitation/deactivation upon irradiation in this part of the spectrum, according to the *ab initio* calculations of Alekseyev and co-workers,[18] and the dashed lines show the Franck-Condon region. As can be inferred from the graph, the extreme sensitivity to the vibrational excitation is related to the details of the crossings between the potential energy surfaces and the spatial distributions of the wave functions at each vibrational level. Therefore, systematic measurements of the properties of this predissociation process provide challenging constraints for theoretical descriptions of this system.

Lifetimes in particular show clearly distinct behavior. Out of those examined, excitation of the $\nu_2 = 1$ level (umbrella mode of CH_3 within the CH_3I molecule; 2_0^1 band) results in the fastest predissociation (average value considering all measurements $\tau = 0.85 \pm 0.04$ ps; see Table II), while the $\nu_3 = 1$ level (one quantum of excitation in the C-I stretch mode; 3_0^1 band) presents the slowest predissociation ($\tau = 4.34 \pm 0.13$ ps; see Table II). It would seem in principle counterintuitive that excitation precisely in ν_3 (the mode of elongation of the C-I bond) corresponds to a slower dissociation. However, as pointed out by Alekseyev *et al.*,[18] *ab initio* calculations show that the $^3A_1$ repulsive state crosses the *B*-band very close to the equilibrium C-I distance of the latter. In this case, the ground state wave function would have a larger

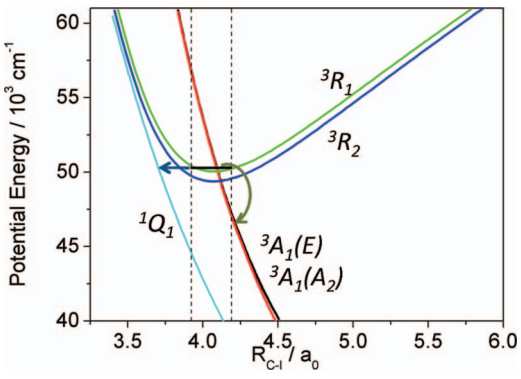

FIG. 14. Potential energy surfaces of CH_3I in the region of 200 nm along the C-I coordinate. The main mechanism for predissociation after excitation in the *B*-band is the interaction with the $^3A_1(4E)$ curve (curved arrow), but decay through the $^1Q_1$ state cannot be ruled out (horizontal arrow), according to the findings of this work (figure adapted from Ref. 18).

overlap with the degenerate continuum state than the $\nu_3 = 1$ level, with a node in the C-I dimension near the position of the curve crossing, which would imply a lower coupling and therefore a slower predissociation. This qualitative description can justify the behavior observed; *ab initio* electronic structure and quantum dynamics calculations are under way in our group to attempt a quantitative explanation.

With regard to the lifetimes measured, it is interesting to compare our results with those reported in Ref. 17 for the 0_0^0 band. In that reference, the authors claim that the observed lifetime measured through the appearance of the CH_3 fragment, is sensitive to the angle between the polarization axis of the probe laser and the C_3 axis of the fragment resulting from dissociation. We have not observed this effect: all lifetimes measured for a given parent excitation (parent decay, iodine appearance, methyl appearance, and photoelectrons) are compatible within errors. Experiments have also been carried out with orthogonal polarizations of the pump and probe lasers, with results that do indicate the existence of fragment alignment (consistent with the results shown in Fig. 2 of Ref. 17), but the lifetimes obtained from those are also consistent with those obtained from Abel-invertible images.

The anisotropy of the iodine atom displays a similar temporal behavior as the predissociation rate; the initial value is found to be -1, which is consistent with the perpendicular character of the transition, and then the β parameter increases to a value that depends on the vibronic level (-0.62 ± 0.05 for the 3_0^1, -0.6 ± 0.1 for 2_0^1, and -0.5 ± 0.1 for 0_0^0). Although the rising times for the anisotropy are always lower than the lifetimes, they turn out to be on the same order, indicating that the evolution of the anisotropy is related to the lifetime of predissociation. It is interesting to note that the slowest band has the higher (in absolute value) final β; this measurement is counter-intuitive and has not been completely understood, since anisotropy is expected to be lost upon rotation of parent molecules in the *B*-band and, and therefore, a more isotropic trend would be expected as the lifetime increases.

As regards final product states, the results obtained for the excitation of CH_3I in the 2_0^1 transition of the *B*-band (i.e., one quantum of excitation in the umbrella mode of the parent CH_3I molecule) can be compared with those that had been reported by us previously for the 0_0^0 band. In both cases, only a single-component, spin-orbit excited $I^*(^2P_{1/2})$ channel is observed, which can be related to the interaction between the bound $^3R_1$ Rydberg state and the repulsive $^3A_1(E)$ state belonging to the *A*-band. However, significant differences have been found in the vibrational excitation in the nascent CH_3 fragment. It is interesting to point out that excitation of the ν_2 mode in the parent molecule does not seem to result in a higher degree of excitation in the ν_2 mode of the methyl fragment, even though these modes are of similar nature (umbrella motion of the CH_3 species). It is possible that the fact that this motion is not "inherited" upon dissociation is related to the different geometry of CH_3 in the molecule (pyramidal) and as an isolated radical (planar), causing largely differing values of the mode energy (1254 cm^{-1} for CH_3I, 606 cm^{-1} for CH_3). Instead, the excess vibrational energy in the parent seems to be channelled into the ν_1 mode of CH_3 (symmetric stretch). Clearly, as can be observed both through iodine and methyl detection, more intense $\nu_1 > 0$ components have been detected. These trends (similar degree of ν_2 excitation and higher degree of ν_1 excitation in nascent CH_3) are shared by the 3_0^1 band ($\nu_3 = 1$ excitation of the parent CH_3I molecule). *Ab initio* potential energy surfaces in two dimensions would be required to explain why excitation of the ν_2 or ν_3 modes of the CH_3I molecule seems to be channelled into symmetric stretch excitation in the CH_3 fragment.

Important information on the nature of the predissociation routes in the *B*-band is derived from the examination of the branching ratio between the spin-orbit excited and the ground-state iodine channels, defined as $\Phi^* = [I^*]/([I] + [I^*])$. Some controversy has existed in the literature over this issue, since values lower than unity had been found in diode laser gain/absorption measurements.[19,33] However, we believe that consensus has been reached in this sense that the diode laser measurements were distorted due to the presence of molecular iodine.[19] All the other previous measurements of this quantity[15,17,18,24,32] have yielded unity, except the recent work by González *et al.*,[34] which will be discussed below. In his very recent theoretical work, Alekseyev and co-workers[18] conclude that the only possibility to obtain $I(^2P_{3/2})$ ground state atoms after *B*-band excitation is by interaction with the repulsive *A*-band $^1Q_1(E)$ state (plotted in Fig. 14), and this would only come into play at excitation energies above 55 000 cm^{-1}. The authors thus conclude that it would be interesting to look for the appearance of ground state $I(^2P_{3/2})$ atoms through excitation around 180 nm.

Our experimental results performed around 200 nm seem to contradict this idea in part. It is true that the branching ratio Φ^* has been found to be unity for the 2_0^1 and 0_0^0 bands. Nevertheless, in the case of 3_0^1 level, methyl fragments that are formed in correlation with $I(^2P_{3/2})$ have been observed, and the direct observation of iodine atoms also shows a shoulder towards higher kinetic energies that we believe to be related to ground state $I(^2P_{3/2})$. As a further test, this component also presents a slow (≈ 4 ps) temporal rise, as the main $I^*(^2P_{1/2})$ component. As was indicated in the Sec. III, through our measurements we obtained an experimental branching ratio for the 3_0^1 band of 0.93 ± 0.05.

From the curves shown in Fig. 14, it is clear that the coupling of the low-lying levels of the $^3R_1$ state with the repulsive $^1Q_1$ state in the region explored in this work must be low. The vibrationless level and the $\nu_2 = 1$ level dissociate strongly via the $^3A_1$ state, as is derived from the fast predissociation times, and this leads to the formation of $I^*(^2P_{1/2})$ only. In contrast, the $\nu_3 = 1$ level shows considerably slower predissociation lifetimes, which, as discussed above, could be related to the lower coupling between this vibronic level of the Rydberg state and the dissociative continuum of the $^3A_1$ state. We believe that this fact opens a window that allows the observation of the channel resulting from the interaction with the $^1Q_1$ state, even at these relatively low excitation energies ($\approx 50\ 000$ cm^{-1}). As is expected, the temporal lifetime observed for this weak channel coincides with that measured for the main $I^*(^2P_{1/2})$ component, since it is determined by the strength of the strongest coupling.

There exists a precedent for this observation of ground-state iodine atom upon *B*-band excitation of CH_3I, and it was

found precisely for excitation to the 3_0^1 band in a nanosecond experiment.[34] In that work, the authors give values of the branching ratio of 0.95±0.01 for the $CH_3(\nu_1 = 1)$ channel, and 1.00 ± 0.01 for the $CH_3(\nu = 0)$ channel. These values are consistent with those found in this work. We believe the consistency between our results and the nanosecond results obtained in Ref. 34 offers strong evidence for the presence of this route in the *B*-band, lowering the threshold from the theoretically expected[18] 55 000 cm^{-1} to 50 223 cm^{-1}. It is possible, however, that this is quite exceptional for the 3_0^1 band, due to the spatial structure of the wavefunction.

Another interesting effect observed only for excitation at 199.2 nm (3_0^1) has been the observation of a minor channel where the fast appearance (<200 fs) of $I^*(^2P_{1/2})$ atoms occurs. This fast component shows similar kinetic energy release (albeit narrower energy distribution) as the main, slow component, but unchanged anisotropy ($\beta \approx -1$). We believe that this fast peak at ≈0.3 eV may be due to fast dissociation of CH_3I upon direct excitation to the dissociative *A*-band. Competition of the weakly absorbing states of the *A*-band would be possible only because of the low absorption cross section of the *B*-band 3_0^1 transition. That the $^3Q_0$ state could be responsible for this absorption can be ruled out not only on energy grounds (unfavorable situation in the Franck-Condon region), but also because of the angular nature of the ion fragment distribution, which has been found to be perpendicular, whereas the $^3Q_0 \leftarrow X^1A$ transition is known to be parallel. We believe that weak absorption either to the $^3A_1(4E)$ state must be responsible for this observation.

V. CONCLUSIONS

A femtosecond pump-probe experiment carried out with the velocity map ion and photoelectron imaging techniques has been employed to obtain a detailed picture of the real-time *B*-band photodissociation in CH_3I. Separate resonant I and CH_3 measurements, together with non-resonant CH_3 probing, have demonstrated that the main channels that are open upon excitation in the 2_0^1 and 3_0^1 bands are $I^*(^2P_{1/2}) + CH_3(\nu_1 = 0, 1, 2; \nu_2 = 0, 1, 2)$. The Φ^* branching ratio, expected to be unity below 55 000 cm^{-1}, was measured to be 1 for the 2_0^1 band but 0.93 ± 0.05 for the 3_0^1 band. Ground state $I(^2P_{3/2})$ is found mainly in correlation with $CH_3(\nu_1 = 1)$. Measurements of the appearance times of all fragment products are compatible within experimental errors, and also with photoelectron and parent molecule decay measurements, and provide values of 0.85 ± 0.04 ps and 4.34 ± 0.13 ps for the lifetimes of the $\nu_2 = 1$ and the $\nu_3 = 1$ levels of the $^3R_1$ state, respectively. Finally, the angular (perpendicular) character of the transition has been determined through real-time detection of the anisotropy observed in the iodine images. The time-dependence of the anisotropy does not seem to be caused completely by molecular rotation as we have obtained unexpected anisotropic distributions for the long-lived 3_0^1 vibronic level. Lifetimes and vibrational activity in the CH_3 product have shown to be very sensitive to the vibrational level initially excited, this being proof of the sensitivity of the interaction strength with the *A*-band surfaces to the detailed structure of each wavefunction. Additionally, a satellite process has been detected for laser excitation at the photon energy corresponding to the 3_0^1 transition, which has been ascribed to a weak absorption to the *A*-band followed by fast direct dissociation.

ACKNOWLEDGMENTS

We thank Dr. J. González-Vázquez and Dr. A. García-Vela for fruitful discussions. M.E.C. acknowledges financial support from MICINN (Spain) through a FPU fellowship. V.L. is grateful for financial support from the JAE-DOC program of CSIC. This work has been financed by the Spanish MICINN through Grant No. CTQ2008-02578, the Consolider program "Science and Applications of Ultrafast Ultraintense Lasers", Grant No. CSD2007-00013, and by the European Union ITN network "Ultrafast control of quantum systems by strong laser fields–FASTQUAST" (Grant No. PITN-GA-2008-214962). This research has been performed within the Unidad Asociada "Química Física Molecular" between Departamento de Química Física of UCM and CSIC. The facilities provided by the Centro de Asistencia a la Investigación de Espectroscopia Multifotónica y de Femtosegundos (UCM) are gratefully acknowledged.

APPENDIX A: MULTIDIMENSIONAL ANALYSIS OF TIME-RESOLVED VELOCITY MAP IMAGING EXPERIMENTS

In general, the analysis of the images acquired in velocity map imaging experiments is carried out using methods that involve cuts or partial integrations through the multidimensional data. As a consequence, in many instances, the full information that can be extracted from the data is not totally and accurately recovered. We have developed a homemade procedure for the complete multidimensional fit of this type of data (examples can be found in recent papers from our group[15,35]) that has proven to be crucial for the extraction of all the relevant information from the images if, in addition, the temporal dimension is included, as it is the case in time-resolved velocity map imaging experiments. This procedure assumes that each image contains the sum of a number of "contributions" (related to each of the mechanisms producing a certain species with a certain velocity distribution). Each contribution is parameterized as a function of all variables (radius and angle for each image, but also time, for instance, to fit a time-dependent series of images) with a test functional form with physical meaning using a sufficient number of adjustable parameters. These first test functions are chosen guided by the known physical properties of the system. A least-squares procedure is then applied to the complete data collection. Inspection of the residuals (typically, also in image format), guides the choice of the second set of functional forms. An iterative procedure of this kind allows the complete parameterization of the data, and from this, quantities such as decay times, anisotropy parameters, etc. can be obtained for each contribution, with estimates of error bars. The procedure and the details of its application to time-resolved

velocity map imaging experiments are presented in more detail in Secs. A 1–A 4 of the Appendix.

1. Numerical fitting procedure

The quality of a 1D-fitting procedure is related to its ability to produce a 1D vector, constructed from a parameterized functional form, to fit a 1D data vector. Typically, the routine optimizes a set of parameters, p_m, of a user-defined functional $F(x; p_m)$, which minimize the global difference between the analytical curve and the data for all values of the x variable. No essential changes are required to fit multidimensional data, since both the elements of the fit matrix $F(x_1, x_2, \ldots, x_n; p_m)$ and those of the experimental data matrix can be sorted in an array (1D), where a global minimization of the difference can be sought. In our case, the minimization algorithm employed is a Levenberg-Marquardt nonlinear regression method.[36–38]

2. Choice of dimensions and global analysis

In the work reported here, the prototype experiment implies the acquisition of a series of velocity map images as a function of time. Therefore, the obvious dimensions for signal parameterization are radius, angle, and time. We would like to stress, however, that more sophisticated schemes can be employed for optimum results. For instance, some of the data shown in this paper have been fitted using four dimensions, where the experimental run has been included as an additional "dimension". Using this strategy, we take into account that some of the parameters (relative intensity of the multiphoton processes, time of temporal overlap, etc.) may have differing values among experimental runs, but some others (decay times, for instance) must retain a given value. Using this approach (artificially "extending" the number of dimensions to include the different measurements of the same quantity) a significant increase of precision is obtained in the determination of crucial values. This is equivalent to using a global analysis procedure for a repeated experiment to determine a given quantity which is common to all experiments.

This strategy has been extensively employed in this work to fit the lifetime of the vibrational levels of the B-state. As an example, the transient of the parent molecule has been measured five times and has been fitted using Eq. (1). The parameters A_1, A_2, τ_{cc}, and t_0 in Eq. (1) can legitimately vary for different runs, but the lifetime τ must be independent from the laser properties. The complete data collection is stored in a matrix as a function of time delay and experimental run. While the laser-dependent parameters are set free to vary for different runs, only a global τ parameter is extracted from all the experiments. This strategy has revealed a high efficiency to decorrelate the value of τ from the laser-dependent parameters.

3. The radial dimension: Kinetic energy distribution

In some cases, only the analysis of the KER is required, in which case integration over the 2π angular range of the images is carried out. In the present work, the measurement of the lifetimes τ of different vibronic levels within the B-band of CH_3I through fragment and photoelectron detection has been carried out considering the KER data as a function of time. The signal $S(v, t)$, depending on speed (v) and time (t), is assumed to be composed of individual contributions $C_i(v, t)$, each of which has its own temporal shape as a function of time, $\Gamma_i(t)$, and speed distribution, $R_i(v)$. It is assumed, in general, that these contributions do not interfere with each other, so that $S(v, t) = \sum_i C_i(v, t)$. Each contribution can typically be simulated by an asymmetric-Gaussian function defined as

$$R(v) = e^{-4\ln 2[(v-v_0)/\sigma_r]^2} H(v-v_0) + e^{-4\ln 2[(v-v_0)/\sigma_l]^2} H(v_0-v), \tag{A1}$$

where v_0 is the position of the peak, σ_r and σ_l are the right and left widths, respectively, and $H(v)$ is the Heaviside function. The physical meaning of the asymmetry in the peaks of the speed distribution is related in most cases to the rotational temperatures of both the parent molecule and the nascent fragment, convoluted by the apparatus response function. The temporal behavior can show different functional forms depending on the type of mechanism, as for instance those described by Eqs. (1) and (2), or a non-resonant MPI detection, which gives a cross-correlation-type signal.

For the cases where no changes in the shape of each contribution are expected as a function of time, we can write

$$C_i(v, t) = \Gamma_i(t) \times R_i(v). \tag{A2}$$

Once the functional forms are defined, a 2D fitting procedure is initiated in order to provide reasonable starting values for the parameters, and later all the experimental data are treated in a unique 3D-fit to include the experimental run as a dimension (see Sec. 2 of Appendix).

4. The angular dimension: Anisotropy

If the analysis of the anisotropy of the time-resolved process is of interest, the angular dimension has to be included in the fitting procedure. If this is the case, the most straightforward strategy is to fit the complete set of Abel-inverted images acquired as a function of time with all the contributions parameterized. However, this would require significant central processing unit time due to the large number of data points (some few tens of millions in a typical case). It is simpler to perform a partial angular integration in 10° steps. Thus, nine speed distributions are extracted from each image corresponding to the different angular ranges. The data are then stored in a 3D matrix with the dimensions speed, angular section, and time.

The time-resolved anisotropy in the angular range centered at θ_0 and with $\Delta\theta$ width is described by partial integration as

$$A(\theta_0, t) \propto \int_{\theta_0 - \frac{\Delta\theta}{2}}^{\theta_0 + \frac{\Delta\theta}{2}} [1 + \beta(t) P_2(\cos\theta)]\, d\theta, \tag{A3}$$

where P_2 is the second-order Legendre polynomial and $\beta(t)$ the time-dependent anisotropy parameter.

The temporal dependence of the anisotropy parameter $\beta(t)$ can be modeled by

$$\beta(t) = \beta^0 + I_r(t) \otimes \Delta\beta[e^{-[(t-t_0)/\tau_\beta]^2} H(t-t_0) + H(t_0-t)], \tag{A4}$$

where β^0 and τ_β are the asymptotic value (long enough delay time) and "relaxation time" of the anisotropy parameter, respectively, $\Delta\beta$ is the amplitude of variation of the exponential decay, and $I_r(t)$ is the system response function. The β values depicted in Figs. 3 and 9 have been evaluated by fitting the data obtained for each temporal step independently after the signal has been cleaned by subtraction of the fit of the other overlapping contributions.

5. Summary

A multidimensional least-squares fitting methodology has been developed for the full analysis of time-resolved velocity map image sequences obtained in femtosecond pump-probe photodissociation experiments. The key advantage of the method consists of its capability to distinguish the different overlapped contributions present in the set of images corresponding to different reaction channels of interest from secondary signals arising from other sources. Moreover, the contributions of interest can be cleanly isolated from the secondary signals by filtering their contributions from the data matrix. The multidimensional fit becomes essential for instance when spatially overlapped contributions are found, which may have different time behavior. Additionally, for those cases where the initial guesses for the parameters or functional forms of the fit are misguided (on the number or nature of the contributions to the image, on the time behavior of anisotropy, etc.), discrepancies can be detected easily through the use of the analysis of the residuals. It is important to note that the multidimensional nature of the fit allows the discrimination of the different contributions to the images, in a manner that a reduced-dimensionality analysis cannot achieve. In addition, there is no conceptual problem to extend the fitting procedure to n dimensions, the only limitation being computational time restrictions to analyze an n-dimensional matrix.

[1] A. Gedanken and M. D. Rowe, Chem. Phys. Lett. **34**, 39 (1975).
[2] R. O. Loo, H.-P. Haerri, G. E. Hall, and P. L. Houston, J. Chem. Phys. **90**, 4222 (1989).
[3] Y. Amatatsu, S. Yabushita, and K. Morokuma, J. Chem. Phys. **104**, 9783 (1996).
[4] A. T. J. B. Eppink and D. H. Parker, J. Chem. Phys. **115**, 4758 (1998).
[5] A. T. J. B. Eppink and D. H. Parker, J. Chem. Phys. **110**, 832 (1999).
[6] R. de Nalda, J. Durá, A. García-Vela, J. G. Izquierdo, J. González-Vázquez, and L. Bañares, J. Chem. Phys. **128**, 244309 (2008).
[7] J. Durá, R. de Nalda, G. A. Amaral, and L. Bañares, J. Chem. Phys. **131**, 134311 (2009).
[8] L. Rubio-Lago, A. García-Vela, A. Arregui, G. Amaral, and L. Bañares, J. Chem. Phys. **131**, 174309 (2009).
[9] M. G. González, J. D. Rodríguez, L. Rubio-Lago, A. García-Vela, and L. Bañares, Phys. Chem. Chem. Phys. **13**, 16404 (2011).
[10] A. P. Baronavski and J. C. Owrustky, J. Chem. Phys. **108**, 3445 (1998).
[11] S. Felps, P. Hochmann, P. Brint, and S. P. McGlynn, J. Mol. Spectrosc. **59**, 355 (1976).
[12] D. J. Donaldson, V. Vaida, and R. Naaman, J. Chem. Phys. **87**, 2522 (1987).
[13] M. R. Dobber, W. J. Buma, and C. A. de Lange, J. Chem. Phys. **99**, 836 (1993).
[14] S. Eden, P. Limão-Vieira, S. V. Hoffmann, and N. J. Mason, Chem. Phys. **331**, 232 (2007).
[15] G. Gitzinger, M. E. Corrales, V. Loriot, R. de Nalda, and L. Bañares, J. Chem. Phys. **132**, 234313 (2010).
[16] N. Thiré, R. Cireasa, V. Blanchet, and S. T. Pratt, Phys. Chem. Chem. Phys. **12**, 15644 (2010).
[17] N. Thiré, R. Cireasa, D. Staedter, V. Blanchet, and S. T. Pratt, Phys. Chem. Chem. Phys. **13**, 18485 (2011).
[18] A. B. Alekseyev, H. P. Liebermann, and R. J. Buenker, J. Chem. Phys. **134**, 044303 (2011).
[19] A. Gilchrist, G. Hancock, R. Peverall, G. Richmond, G. A. D. Ritchie, and S. Taylor, J. Phys. Chem. A **112**, 4531 (2008).
[20] P. G. Wang, Y. P. Zhang, C. J. Ruggles, and L. D. Ziegler, J. Chem. Phys. **92**, 2806 (1990).
[21] L. D. Ziegler, Y. C. Chung, P. G. Wang, and Y. P. Zhang, J. Phys. Chem. **94**, 3394 (1990).
[22] P. G. Wang and L. D. Ziegler, J. Chem. Phys. **95**, 288 (1991).
[23] J. A. Syage, Chem. Phys. Lett. **212**, 124 (1993).
[24] R. E. Continetti, B. A. Balko, and Y. T. Lee, J. Chem. Phys. **89**, 3383 (1988).
[25] G. A. García, L. Nahon, and I. Powis, Rev. Sci. Instrum. **75**, 4989 (2004).
[26] R. N. Zare, *Angular Momentum. Understanding Spatial Aspects in Chemistry and Physics* (Wiley, New York, 1998).
[27] V. A. Shubert, M. Rednic, and S. T. Pratt, J. Chem. Phys. **130**, 134306 (2009).
[28] C. Jonah, J. Chem. Phys. **55**, 1915 (1971).
[29] S. Yang and R. Bersohn, J. Chem. Phys. **61**, 4400 (1974).
[30] L. Karlsson, R. Jadrny, L. Mattsson, F. T. Chau, and K. Siegbahn, Phys. Scr. **16**, 225 (1977).
[31] A. Strobel, I. Fischer, A. Lochschmidt, K. Müller-Dethlefs, and V. E. Bondybey, J. Phys. Chem. **98**, 2024 (1994).
[32] G. N. A. van Veen, T. Baller, and A. E. de Vries, Chem. Phys. **97**, 179 (1985).
[33] W. P. Hess, R. Naaman, and S. R. Leone, J. Phys. Chem. **91**, 6085 (1987).
[34] M. G. González, J. D. Rodríguez, L. Rubio-Lago, and L. Bañares, J. Chem. Phys. **135**, 021102 (2011).
[35] R. de Nalda, J. Durá, J. González-Vázquez, V. Loriot, and L. Bañares, Phys. Chem. Chem. Phys. **13**, 13295 (2011).
[36] D. W. Marquardt, SIAM J. Appl. Math. **11**, 431 (1963).
[37] Y. Bard, *Nonlinear Parameter Estimation* (Academic, New York, 1974).
[38] N. R. Draper and H. Smith, *Applied Regression Analysis (Wiley Series in Probability and Statistics)* (Wiley, New York, 1981).
[39] See supplementary material at http://dx.doi.org/10.1063/1.3683252 for the time dependence of the β_2 and β_4 anisotropy parameters. Panels (a) and (b) correspond to CH_3I^+ photoelectrons from excitation to the origin and 3_0^1 bands, respectively. Panels (c) and (d) correspond to I^+ photoelectron from excitation to the origin and 3_0^1 bands, respectively.